



WHY IS A FLARE-RICH ACTIVE REGION CME-POOR?

LIJUAN LIU^{1,2}, YUMING WANG^{1,3}, JINGXIU WANG⁴, CHENGLONG SHEN^{1,3}, PINZHONG YE¹, RUI LIU^{1,2}, JUN CHEN^{1,5},
QUANHAO ZHANG^{1,5}, AND S. WANG^{1,2}

¹ CAS Key Laboratory of Geospace Environment, Department of Geophysics and Planetary Sciences, University of Science and Technology of China, Hefei, Anhui 230026, China; ymwang@ustc.edu.cn, ljliu@mail.ustc.edu.cn

² Collaborative Innovation Center of Astronautical Science and Technology, China

³ Synergetic Innovation Center of Quantum Information & Quantum Physics, University of Science and Technology of China, Hefei, Anhui 230026, China

⁴ National Astronomical Observatories, Chinese Academy of Sciences, Beijing 100012, China

⁵ Mengcheng National Geophysical Observatory, University of Science and Technology of China, China

Received 2015 February 17; revised 2016 May 10; accepted 2016 May 11; published 2016 July 26

ABSTRACT

Solar active regions (ARs) are the major sources of two of the most violent solar eruptions, namely flares and coronal mass ejections (CMEs). The largest AR in the past 24 years, NOAA AR 12192, which crossed the visible disk from 2014 October 17 to 30, unusually produced more than one hundred flares, including 32 M-class and 6 X-class ones, but only one small CME. Flares and CMEs are believed to be two phenomena in the same eruptive process. Why is such a flare-rich AR so CME-poor? We compared this AR with other four ARs; two were productive in both and two were inert. The investigation of the photospheric parameters based on the *SDO*/HMI vector magnetogram reveals that the flare-rich AR 12192, as with the other two productive ARs, has larger magnetic flux, current, and free magnetic energy than the two inert ARs but, in contrast to the two productive ARs, it has no strong, concentrated current helicity along both sides of the flaring neutral line, indicating the absence of a mature magnetic structure consisting of highly sheared or twisted field lines. Furthermore, the decay index above the AR 12192 is relatively low, showing strong constraint. These results suggest that productive ARs are always large and have enough current and free energy to power flares, but whether or not a flare is accompanied by a CME is seemingly related to (1) the presence of a mature sheared or twisted core field serving as the seed of the CME, or (2) a weak enough constraint of the overlying arcades.

Key words: Sun: activity – Sun: coronal mass ejections (CMEs) – Sun: flares – Sun: magnetic fields

1. INTRODUCTION

Both solar flares and coronal mass ejections (CMEs) indicate the rapid release of a huge amount of magnetic energy in the solar corona; CMEs, in particular, are the most important driving source of hazardous space weather near the geospace. As the major producer of flares and CMEs, active regions (ARs) have been studied for decades. Substantial observational studies have revealed that parameters characterizing the AR's non-potentiality, e.g., shear length, magnetic gradient, total electric current, or free energy, are all correlated with flare and CME productivity (e.g., Canfield et al. 1999; Sammis et al. 2000; Falconer et al. 2002, 2006; Leka & Barnes 2003b, 2003a; Jing et al. 2006; Ternullo et al. 2006; Georgoulis & Rust 2007; Guo et al. 2007; Schrijver 2007; Wang & Zhang 2008), and larger ARs in particular are more likely to produce eruptions (e.g., Tian et al. 2002; Chen et al. 2011). However, not all large ARs have similar productivities in flares and CMEs, and some may be productive in flares only (e.g., Tian et al. 2002; Akiyama et al. 2007; Chen & Wang 2012). How to distinguish the productivity of an AR is a key issue in space weather forecasting, and one that remains unsolved.

The recent super AR, 12192, which crossed the visible solar disk during 2014 October 17–30, received considerable attention (*RHESSI* science nugget no.239; Sun et al. 2015; Thalmann et al. 2015). Despite being the largest AR since 1990 November, it produced only one small CME although a total of 127 C-class and more intense flares, including 32 M-class and 6 X-class ones, were generated. Flares and CMEs are thought to be the consequences of the same eruptive process (e.g.,

Harrison 1995; Lin & Forbes 2000). Although the amount of energy they release during a strong eruption is on the same order of about 10^{32} erg (Emslie et al. 2012), they are clearly different. Flares are relatively local phenomena, and the released energy is mostly converted into radiation and energetic particles; CMEs are more global phenomena, and the energy mostly goes into mechanical energies through the ejection of magnetized plasma structures. An intense flare may not necessarily be accompanied by a CME (e.g., Feynman & Hundhausen 1994; Green et al. 2002b; Yashiro et al. 2005; Wang & Zhang 2007), because the occurrence of a CME is substantially determined by the driving force of the inner core magnetic field and the confining force of the external overlying field (e.g., Wang & Zhang 2007; Liu 2008; Schrijver 2009).

The inner driver always takes the form of a highly sheared or twisted magnetic structure, e.g., a flux rope as required in most CME models (Amari et al. 1999; Török & Kliem 2005). A sheared or twisted field carries magnetic helicity, and thus provides a way to transport helicity naturally (Low 1994; Amari et al. 1999). Since magnetic helicity is invariant in the highly conductive corona, it is notable that a CME may be an inevitable product of the accumulation of helicity in the corona (Low 1994; Green et al. 2002a; Nindos et al. 2003; Zhang 2006; Zhang et al. 2006; Zhang & Flyer 2008; Liu & Schuck 2012; Valori et al. 2012).

An AR of continuously generating M- and X-class flares without a strong CME such as this one has rarely been noticed. In particular, three out of six non-CME X-class flares were of long duration (lasting more than one hour), which contradicts many earlier studies showing that long-duration flares tend to erupt out more easily (e.g., Harrison 1995; Yashiro et al. 2006).

Table 1
Information and Parameters of the ARs

NOAA	11157	11158	11428	11429	12192
Hemisphere	North	South	South	North	South
Date on the visible disk	20110208-0217	20110211-0221	20120302-0313	20120303-0315	20141018-1030
Productivity	Inert	Flare-CME-rich	Inert	Flare-CME-rich	Flare-rich only
Φ (10^{22} Mx)	0.55 ± 0.25	1.88 ± 1.09	1.25 ± 0.11	5.58 ± 0.23	15.01 ± 2.06
ρ_{tot} (10^{23} erg cm $^{-1}$)	0.44 ± 0.30	4.97 ± 3.34	2.05 ± 0.78	13.88 ± 2.64	48.65 ± 4.87
I_{total} (10^{13} A)	0.97 ± 0.35	4.08 ± 2.19	2.43 ± 0.35	9.45 ± 1.20	22.28 ± 1.57
$\overline{H_c}$ (10^{-3} G 2 m $^{-1}$)	-4.62 ± 4.69	13.11 ± 9.98	-3.69 ± 4.31	-22.27 ± 4.88	-3.24 ± 1.75
H_{ctotal} (10^3 G 2 m $^{-1}$)	0.42 ± 0.17	2.19 ± 1.20	0.98 ± 0.16	4.76 ± 0.81	12.17 ± 0.99

Note. The lower five rows show the mean values and the standard deviations of the quantities during the period in which the CMD was within $\pm 45^\circ$. See Table 3 for the formulas of the parameters.

In order to understand the underlying physical nature, we compared this super AR with two other pairs of ARs (11157 and 11158, and 11428 and 11429) in the first section, and then investigated the temporal evolution of photospheric parameters, pre-flare distribution of current helicity, and decay index of the five ARs in the next two sections. In the final section, we provide a summary and discussion.

2. ACTIVITIES OF THE ARs

The ARs 11157 and 11158 were chosen for comparison because their productivities are quite different and because they transited the visible solar disk during almost the same time; ARs 11428 and 11429 were chosen for the same reasons.

AR 11157 was a very poor AR, and no flare or CME was generated during its visible disk passage. In contrast, AR 11158 produced 68 flares above C1.0 and 12 CMEs, 10 of which were associated with flares above C1.0. AR 11429, similar to AR 11158, was also prolific. It produced 64 flares above C1.0 and 16 CMEs, 10 of which were flare-accompanied. AR 11428 was chosen as a comparison for 11429, as it produced only five C-class flares without any CME. It is noteworthy that AR 11429 and its neighbor AR 11430 were clustered, they exhibited a close magnetic connection with each other, and some weaker flares simultaneously occurred in AR 11430 when AR 11429 generated flares; the SHARP (Space weather HMI Active Region Patches) cutout maps of vector magnetograms that contain a single AR or a cluster of ARs (Bobra et al. 2014; Hoeksema et al. 2014)) data also contains the two ARs. Therefore, here we simply treat them as an AR complex. Information about the ARs is shown in Table 1. The associations of flares, CMEs, and ARs are checked manually using *GOES* 1.0–8.0 Å soft X-Ray flux data and the imaging data from *SOHO*/LASCO (Brueckner et al. 1995), *STEREO*/COR (Kaiser et al. 2008), and *SDO*/AIA (Lemen et al. 2012).

For clarity, Figure 1 shows the *GOES* soft X-Ray (SXR) flux during these ARs' transits. ARs 11157 and 11158 share the same light curve of the *GOES* SXR, as do ARs 11428 and 11429. To distinguish the eruptions from the ARs, we used different colors for different ARs. In the figure, all the associated flares are indicated by colored lines and the associated CMEs are marked by arrows. All the flares above M1.0 and the CMEs have been listed in Table 2. The parameters of the flares are taken from the SolarMonitor⁶, which is generated based on NOAA active region summaries, and the parameters of the CMEs are taken from the *SOHO*/

LASCO CME Catalog⁷ (Yashiro 2004) and the *SECCHI*/COR2 CME Catalog⁸ (Olmedo et al. 2008).

3. TEMPORAL EVOLUTION OF THE PHOTOSPHERIC PARAMETERS

Considering that an eruption, i.e., a flare or a CME, only lasts for a relatively short duration and an AR is not always active, we suggest that the overall features of the parameters during a noticeable duration may be more appropriate for characterizing an AR's total productivity than instant values, although instant values are more valuable for the prediction of a single event. Based on this idea, we carefully checked the temporal evolution of all the SHARP parameters based on photospheric vector magnetograms (Bobra et al. 2014). As indicated by the vertical dashed lines in Figure 1, the duration during which the central meridian distance (CMD) of the AR's geometric center is within $\pm 45^\circ$ was chosen to avoid the low signal-to-noise of the data near the solar limb.

We first found that three parameters, the total magnetic flux (Φ), the total unsigned vertical current (I_{total}), and the proxy of photospheric free magnetic energy (ρ_{tot}), may be useful in distinguishing ARs of different flare productivities. Since their evolutionary trends are similar, only ρ_{tot} is shown in Figure 2(a). The formal random error from the determination of the vector field is overplotted as error bars, which are smaller compared to the values of the parameters themselves. Detailed formulas of the parameters are listed in Table 3.

It is obvious that the two flare-rich ARs, 11429 and 12192, have larger ρ_{tot} than the two inert ARs over their entire duration. The ρ_{tot} value of the other prolific AR, 11158, is small until it reaches the central meridian since it is a newly emerged AR. There was no intense flare from the AR until ρ_{tot} became large, as shown by the purple hollow arrows in Figure 2(a). The mean values of Φ , I_{total} , and ρ_{tot} of ARs 11158, 11429, and 12192 during the duration, as shown in Table 1, are also larger than those of the two inert ones. The results are consistent with the well-known picture that total flux is a physical measure of the size of an AR, reflecting the total magnetic energy contained in the AR; the electric current describes the deviation of the magnetic field from potential configuration, referring to the accumulation of free energy. The rapid dissipation of current could be manifested by flares, thus the strong current system seems to be a favorable condition for flares.

⁶ <http://www.solarmonitor.org/>

⁷ http://cdaw.gsfc.nasa.gov/CME_list/

⁸ <http://spaceweather.gmu.edu/seeds/secchi.php>

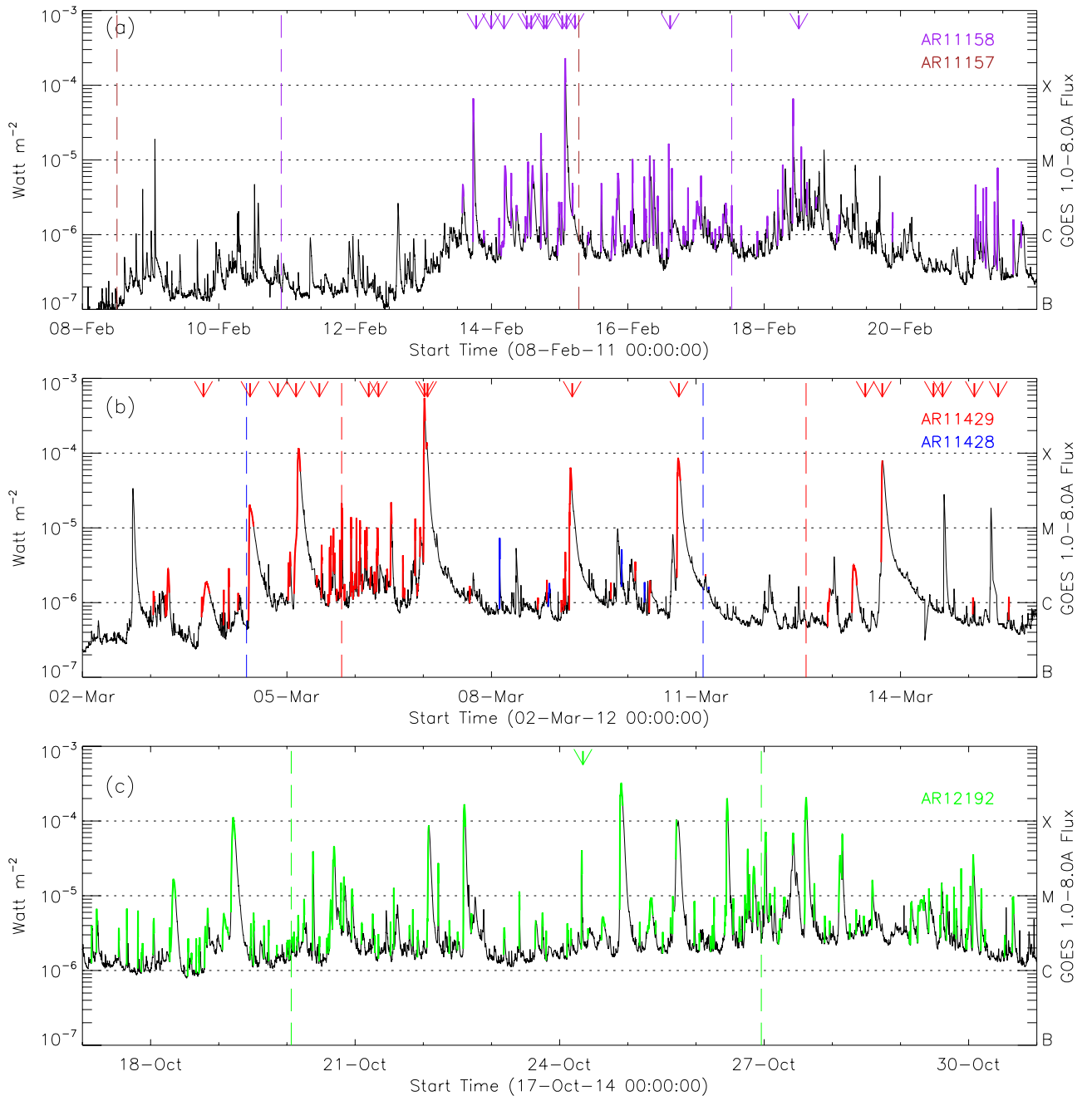


Figure 1. GOES soft X-Ray light curves during the ARs' disk passage, panel (a) for ARs 11157 and 11158, (b) for ARs 11428 and 11429, and (c) for AR 12192. Superimposed colored lines indicate the associated flares; brown, purple, blue, red, and green colors represent AR 11157, 11158, 11428, 11429, and 12192, respectively. CMEs originating from the corresponding ARs are marked by arrows. Vertical dashed lines indicate the time window when the central meridian distance (CMD) of the ARs' geometric centers were within $\pm 45^\circ$.

It is hard to tell which parameter is more critical. As shown in many previous studies, the combination of the three parameters is responsible for the flare productivity (Leka & Barnes 2007). In fact, such a combination of sharp parameters has been used for flare prediction: employing a machine-learning algorithm, a set of quantities that mostly describe the magnetic energy and vertical current, can achieve a relatively high ability to distinguish flaring and non-flaring ARs (Bobra & Couvidat 2015).

We also find another parameter, mean current helicity ($\overline{H_c}$), being very consistent with the CME productivity, as shown in Figure 2(b). Although AR 12192 is the largest AR, its mean

current helicity ($\overline{H_c}$) is comparable to that of the two inert ARs, and smaller than that of the two CME-rich ARs.

Quantities describing current helicity are sometimes used as photospheric proxies of magnetic helicity (e.g., Seehafer 1990; Abramenko et al. 1996; Bao & Zhang 1998; Zhang & Bao 1998; Zhang et al. 2000; Wang & Zhang 2015). Magnetic helicity, defined as $H_m = \int A \cdot B dx^3$, reflecting the twist, shear, linking, or other non-potential properties of the magnetic field, is approximately conserved in nearly ideal MHD circumstance, e.g., the atmosphere of the Sun (Berger & Field 1984; Pevtsov et al. 1995; Brown et al. 1999, p. 111; Low & Berger 2003; Démoulin 2007; Pevtsov et al. 2014). Excess H_m injected into

Table 2
Flares and CMEs from ARs 11158, 11429, and 12192a

AR No.	No.	Flares					CMEs		
		Date	Begin (UT)	End (UT)	Peak (UT)	Class	Time ^b (UT)	Width (degree)	Speed (km s ⁻¹)
11158	1	2011/Feb/13	17:28:00	17:47:00	17:38:00	M6.6	18:36:05	276	373
	2	2011/Feb/13	23:54:00	73	370 ^c
	3	2011/Feb/14	04:29:00	05:09:00	04:49:00	C8.3	04:24:00	68	384 ^c
	4	2011/Feb/14	11:51:00	12:26:00	12:00:00	C1.7	12:24:00	61	810 ^c
	5	2011/Feb/14	13:47:00	14:42:00	14:27:00	C7.0	14:00:07	22	380
	6	2011/Feb/14	17:20:00	17:32:00	17:26:00	M2.2	18:24:05	360	326
	7	2011/Feb/14	19:23:00	19:36:00	19:30:00	C6.6	19:24:00	81	349 ^c
	8	2011/Feb/15	00:31:00	00:48:00	00:38:00	C2.7	00:54:00	82	1843 ^c
	9	2011/Feb/15	01:44:00	02:06:00	01:56:00	X2.2	02:24:05	360	669
	10	2011/Feb/15	04:27:00	04:37:00	04:32:00	C4.8	05:24:00	104	1748 ^c
	11	2011/Feb/16	01:32:00	01:46:00	01:39:00	M1.0
	12	2011/Feb/16	07:35:00	07:44:00	07:44:00	M1.1
	13	2011/Feb/16	14:19:00	14:29:00	14:25:00	M1.6	14:54:00	75	320 ^c
	14	2011/Feb/18	09:55:00	10:15:00	10:11:00	M6.6
	15	2011/Feb/18	12:12:05	89	350
	16	2011/Feb/18	12:59:00	13:06:00	13:03:00	M1.4
11429	1	2012/Mar/03	17:56:00	18:05:00	18:03:00	C1.1	18:36:05	192	1078
	2	2012/Mar/04	10:29:00	12:16:00	10:52:00	M2.0	11:00:07	360	1306
	3	2012/Mar/04	20:48:05	50	720
	4	2012/Mar/05	02:30:00	04:43:00	04:05:00	X1.1	03:12:09	92	594
	5	2012/Mar/05	11:24:06	50	428
	6	2012/Mar/05	19:10:00	19:21:00	19:16:00	M2.1
	7	2012/Mar/05	19:27:00	19:32:00	19:30:00	M1.8
	8	2012/Mar/05	22:26:00	22:42:00	22:34:00	M1.3
	9	2012/Mar/06	00:22:00	00:31:00	00:28:00	M1.3
	10	2012/Mar/06	01:36:00	01:50:00	01:44:00	M1.2
	11	2012/Mar/06	04:01:00	04:08:00	04:05:00	M1.0	04:48:06	111	536
	12	2012/Mar/06	07:52:00	08:00:00	07:55:00	M1.0	08:12:08	107	599
	13	2012/Mar/06	12:23:00	12:54:00	12:41:00	M2.1
	14	2012/Mar/06	21:04:00	21:14:00	21:11:00	M1.3
	15	2012/Mar/06	22:49:00	23:11:00	22:53:00	M1.0
	16	2012/Mar/07	00:02:00	00:40:00	00:24:00	X5.4	00:24:06	360	2684
	17	2012/Mar/07	01:05:00	01:23:00	01:14:00	X1.3	01:30:24	360	1825
	18	2012/Mar/09	03:22:00	04:18:00	03:53:00	M6.3	04:26:09	360	950
	19	2012/Mar/10	17:15:00	18:30:00	17:46:00	M8.4	18:00:05	88	491
	20	2012/Mar/13	11:36:05	54	229
	21	2012/Mar/13	17:12:00	17:41:00	17:30:00	M7.9	17:36:05	360	1884
	22	2012/Mar/14	11:36:05	11	565
	23	2012/Mar/14	14:48:05	28	533
	24	2012/Mar/15	02:00:05	74	318
	25	2012/Mar/15	10:24:05	31	388
12192	1	2014/Oct/18	07:02:00	08:49:00	07:58:00	M1.6
	2	2014/Oct/19	04:17:00	05:48:00	05:03:00	X1.1
	3	2014/Oct/20	09:00:00	09:20:00	09:11:00	M3.9
	4	2014/Oct/20	16:00:00	16:55:00	16:37:00	M4.5
	5	2014/Oct/20	18:55:00	19:04:00	19:02:00	M1.4
	6	2014/Oct/20	19:53:00	20:13:00	20:03:00	M1.7
	7	2014/Oct/20	22:43:00	23:13:00	22:55:00	M1.2
	8	2014/Oct/21	13:35:00	13:40:00	13:38:00	M1.2
	9	2014/Oct/22	01:16:00	01:59:00	01:59:00	M8.7
	10	2014/Oct/22	05:11:00	05:21:00	05:17:00	M2.7
	11	2014/Oct/22	14:02:00	14:50:00	14:28:00	X1.6
	12	2014/Oct/23	09:44:00	09:56:00	09:50:00	M1.1
	13	2014/Oct/24	07:37:00	07:53:00	07:48:00	M4.0	08:00:05	96	677
	14	2014/Oct/24	21:07:00	22:13:00	21:40:00	X3.1
	15	2014/Oct/25	16:55:00	17:08:00	17:08:00	X1.0
	16	2014/Oct/26	10:04:00	11:18:00	10:56:00	X2.0
	17	2014/Oct/26	17:08:00	17:30:00	17:17:00	M1.0

Table 2
(Continued)

AR No.	No.	Flares					CMEs		
		Date	Begin (UT)	End (UT)	Peak (UT)	Class	Time ^b (UT)	Width (degree)	Speed (km s ⁻¹)
	18	2014/Oct/26	18:07:00	18:20:00	18:15:00	M4.2
	19	2014/Oct/26	18:43:00	18:56:00	18:49:00	M1.9
	20	2014/Oct/26	19:59:00	20:45:00	20:21:00	M2.4
	21	2014/Oct/27	00:06:00	00:44:00	00:34:00	M7.1
	22	2014/Oct/27	01:44:00	02:11:00	02:02:00	M1.0
	23	2014/Oct/27	03:35:00	03:48:00	03:41:00	M1.3
	24	2014/Oct/27	09:59:00	10:26:00	10:09:00	M6.7
	25	2014/Oct/27	14:12:00	15:09:00	14:47:00	X2.0
	26	2014/Oct/27	17:33:00	17:47:00	17:40:00	M1.4
	27	2014/Oct/28	02:15:00	03:08:00	02:41:00	M3.4
	28	2014/Oct/28	03:23:00	03:41:00	03:32:00	M6.6
	29	2014/Oct/28	13:54:00	14:23:00	14:06:00	M1.6
	30	2014/Oct/29	06:03:00	08:20:00	08:20:00	M1.0
	31	2014/Oct/29	09:54:00	10:06:00	10:01:00	M1.2
	32	2014/Oct/29	14:24:00	14:33:00	14:33:00	M1.4
	33	2014/Oct/29	16:06:00	16:33:00	16:20:00	M1.0
	34	2014/Oct/29	18:47:00	18:52:00	18:50:00	M1.3
	35	2014/Oct/29	21:18:00	21:25:00	21:22:00	M2.3
	36	2014/Oct/30	00:34:00	00:40:00	00:37:00	M1.3
	37	2014/Oct/30	01:19:00	01:56:00	01:35:00	M3.5
	38	2014/Oct/30	04:17:00	04:36:00	04:28:00	M1.2

Notes.

^a Blanks in the flare (CME) column mean that no C-class or more intense flare (CME) is associated with the CME (flare).

^b First appearance in the field of view of the *SOHO*/LASCO C2 or the *STEREO*/COR2 (missed by C2).

^c CMEs recorded by COR2.

the corona could be reorganized by locally resistant activities, finally erupting out in the form of a highly sheared or twisted core field (e.g., flux ropes) contained in CMEs. It is notable that ARs with eruptive flares contain more coronal magnetic helicity than the ones with confined flares (Nindos & Andrews 2004; Tziotziou et al. 2012). In the nearly force-free state, the currents are almost parallel to the magnetic field lines; therefore, the helicity of current could be a proxy of magnetic helicity.

However, the mean current helicity ($\overline{H_c}$) that we used above is a signed average. On the one hand, the large value of $\overline{H_c}$ does indicate the presence of a highly sheared or twisted field; on the other hand, the small value of $\overline{H_c}$ could be the result of either the absence of a highly sheared or twisted field or the offset between two highly sheared or twisted fields with opposite handedness. Thus an additional parameter, total unsigned current helicity $H_{c\text{total}}$, has been checked to find the reason for the small $\overline{H_c}$ of the three CME-poor ARs. As shown in Figure 2(c), ARs 11157 and 11428 both have a small $H_{c\text{total}}$, but AR 12192 has quite a large $H_{c\text{total}}$, which means that there may be some sheared or twisted fields in AR 12192 as well. Pre-existing, highly sheared, or twisted core fields could serve as a seed structure for a CME, so why is AR 12192 still CME-poor? The position and the maturity of the core field and the confinement above the AR may be responsible. In order to examine this speculation further, we investigated the spatial distribution of the current helicity on the photosphere and the decay index of the magnetic field above the ARs in the next section.

4. PRE-FLARE CONDITIONS

4.1. Spatial Distribution of Current Helicity

We inspected the spatial distribution of the current helicity h_c on the photosphere of the ARs at specific moments. These are the central meridian transits for the two inert ARs, 11157 and 11428, and the moments right before the onsets of the largest flares of the three productive ARs: the X2.2 (2011-02-15T01:44) flare for 11158, the X5.4 (2012-03-07T00:02) flare for 11429, and the X3.1 (2014-10-24T21:07) flare for 12192. The former two flares are eruptive, and the last one is confined.

Figure 3 shows the vector magnetic field at the specific moments of the five ARs. The B_r component is plotted as background in a dynamic range of ± 1000 Gauss, with white (black) patches for the positive (negative) B_r . Orange (blue) arrows show the horizontal field component that originates from the positive (negative) B_r region. The panels are plotted in units of Mm with the same scale, allowing direct comparison of the size of the ARs. Clearly AR 12192 is the largest one, having as strong a magnetic field as the other two productive ARs. It should be noted that there are some “bad pixels” with abnormally weak B_r in the center of the negative polarity of AR 12192, which may be a result of failed inversion. We set thresholds on both the values of formal errors and relative errors to the vector magnetic field, located those pixels, and smoothed them with ambient pixels. Current helicity was calculated after the smoothing. In each pixel, it is calculated by the formula $h_c = B_z \cdot (\nabla \times B)_z = \mu_0 B_z J_z$, in which the vertical current density J_z is weighted by B_z , the vertical component of magnetic field, which makes h_c more sensitive to

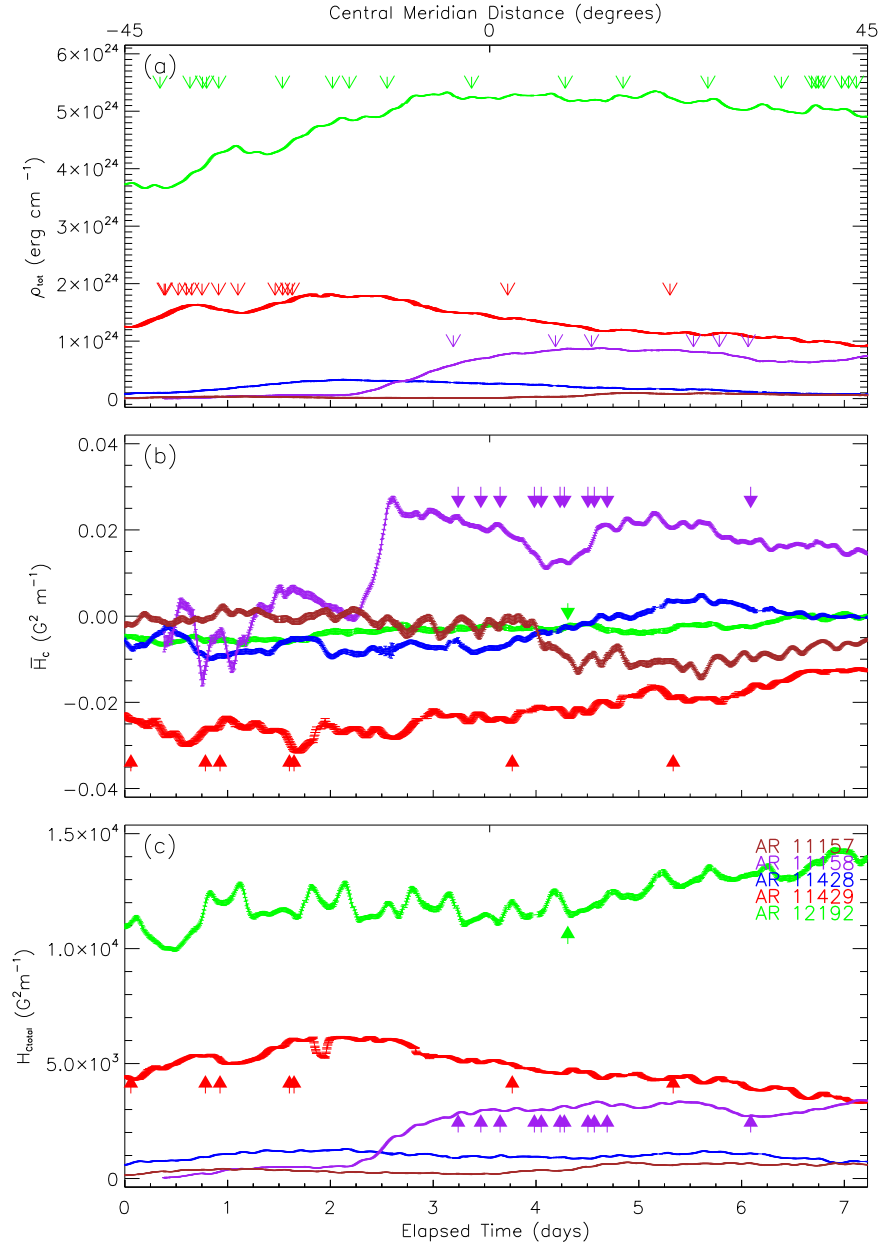


Figure 2. The evolution of proxy of photospheric free magnetic energy ρ_{tot} (in panel (a)), mean current helicity \overline{H}_c (in panel (b)), and total unsigned current helicity $H_{c,\text{total}}$ (in panel (c)); the hollow arrows in panel (a) indicate associated flares more severe than M-class; the solid arrows in panel (b) and (c) are for CMEs; the brown, purple, blue, red, and green colors are for AR 11157, 11158, 11428, 11429, and 12192, respectively.

Table 3
Parameters Used to Distinguish the AR's Productivity^a

Parameters	Description	Unit	Formula	Statistic
Φ	Total unsigned flux	Mx	$\Phi = \sum B_z dA$	Integral
ρ_{tot}	Proxy for total photospheric Excess magnetic energy	erg cm^{-1}	$\rho_{\text{tot}} = \sum \frac{1}{8\pi} (B^{\text{obs}} - B^{\text{Pot}})^2 dA$	Integral
I_{total}	Total unsigned vertical current	A	$I_{\text{total}} = \sum J_z dA$	Integral
\overline{H}_c	Mean current helicity (B_z contribution)	$\text{G}^2 \text{m}^{-1}$	$\overline{H}_c = \frac{1}{N} \sum B_z (\nabla \times B)_z$	Mean
$H_{c,\text{total}}$	Total unsigned current helicity	$\text{G}^2 \text{m}^{-1}$	$H_{c,\text{total}} = \sum B_z (\nabla \times B)_z $	Sum

Note.

^a Adapted from Bobra et al. (2014). Here $\mu_0 J_z = (\nabla \times B)_z = \left(\frac{\partial B_y}{\partial x} - \frac{\partial B_x}{\partial y} \right)$.

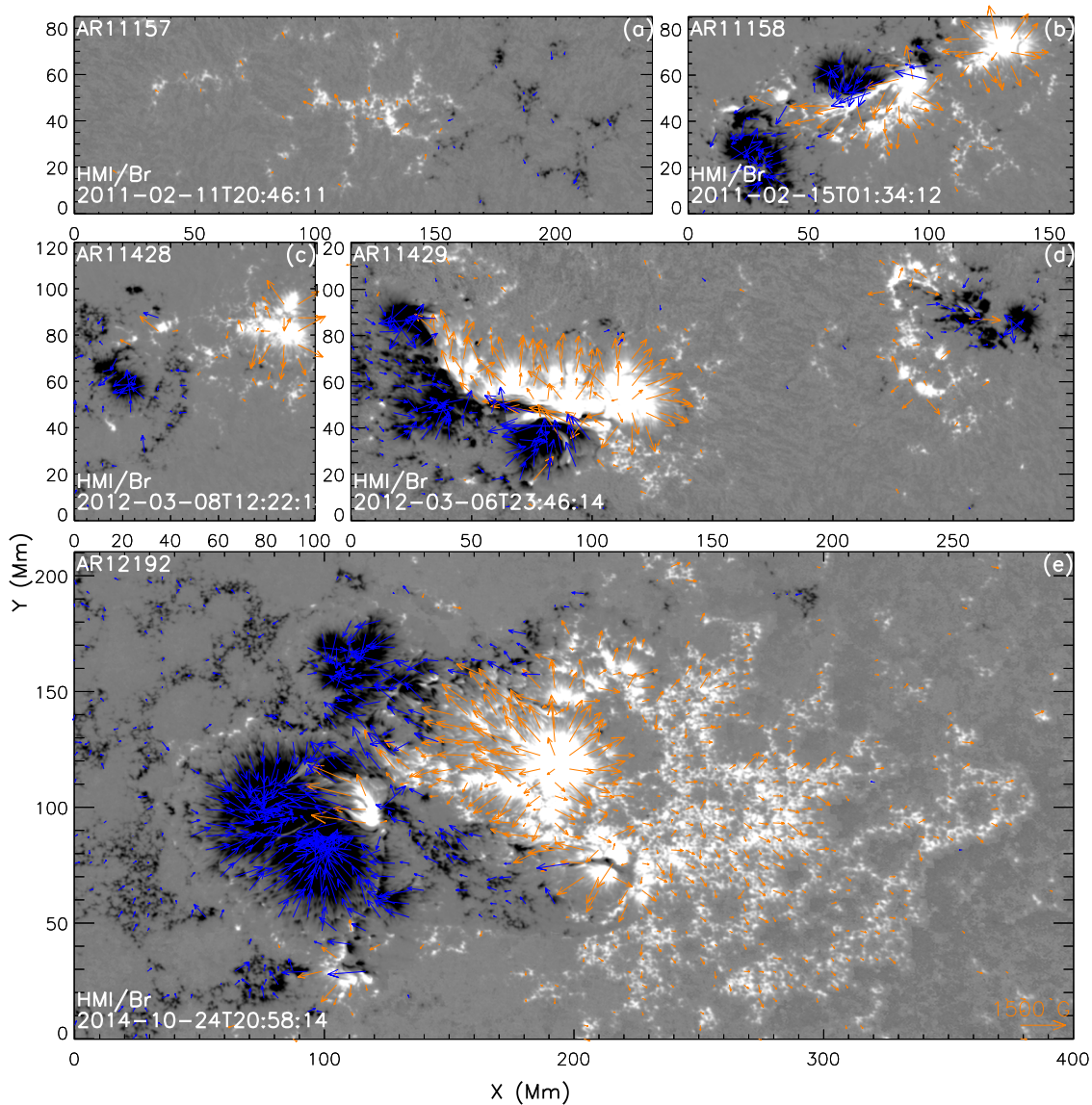


Figure 3. Vector magnetic field at the specific moments of the five ARs, panels (a)–(e) are for AR 11157, 11158, 11428, 11429, and 12192, respectively. The background is B_z component plotted in a dynamic range of ± 1000 Gauss, with white (black) regions for the positive (negative) B_z . Orange (blue) arrows show the horizontal field component that originates from the positive (negative) B_z region.

the twist or shear of the vertical field under the force-free assumption.

Colored patches in Figure 4 show the distribution of current helicity, red for the regions of $h_c \geq 0.3 \text{ G}^2 \text{ m}^{-1}$ and green for $h_c \leq -0.3 \text{ G}^2 \text{ m}^{-1}$; the threshold of $\pm 0.3 \text{ G}^2 \text{ m}^{-1}$ is about two times the standard deviation from the mean value of the h_c map of AR 12192, in which can be found regions of extremely large h_c . In the background are images of *AIA*/1600 Å near the flares’ peaks, showing the positions of the flare ribbons. The B_z component of the field is contoured on the images: orange contours for a positive B_z of 200, 1000 Gauss, blue contours for a negative B_z of -200 , -1000 Gauss.

The black dotted lines indicate the neutral lines where the flares originated, if any. One may expect the flare of AR 12192 to be mainly associated with the positive polarity within the major negative-polarity concentration, but the flare did light along the neutral line indicated by the black dotted line, as shown by the flare ribbons in Figure 4(e); this is also confirmed in Thalmann’s work (Thalmann et al. 2015). It is clear that in

each of the two ARs with eruptive flares, AR 11158 and 11429, there is strong, concentrated current helicity along both sides of the neutral lines associated with the flare ribbons; while almost no strong current helicity exists in the two inert ARs, 11157 and 11428. In the AR with a confined flare, AR 12192, strong, concentrated current helicity exists predominantly in the largest negative polarity spot, far from the flaring neutral line.

The concentrated patches of strong current helicity along the flaring neutral line may indicate the photospheric footprints of the highly sheared or twisted core field that may serve as the seed of a CME. We think that the field lines for a mature core field should come out from a strong h_c region of the positive polarity, and go into a strong h_c region of the negative polarity, which means that there should be strong h_c regions in both the positive and negative polarities on the photosphere. Then one may expect the magnetic flux in the positive and negative polarity patches with strong h_c to be roughly balanced. Thus we propose a ratio (R^ϕ) between the magnetic flux contributed by the strong h_c regions in both polarities to test this speculation.

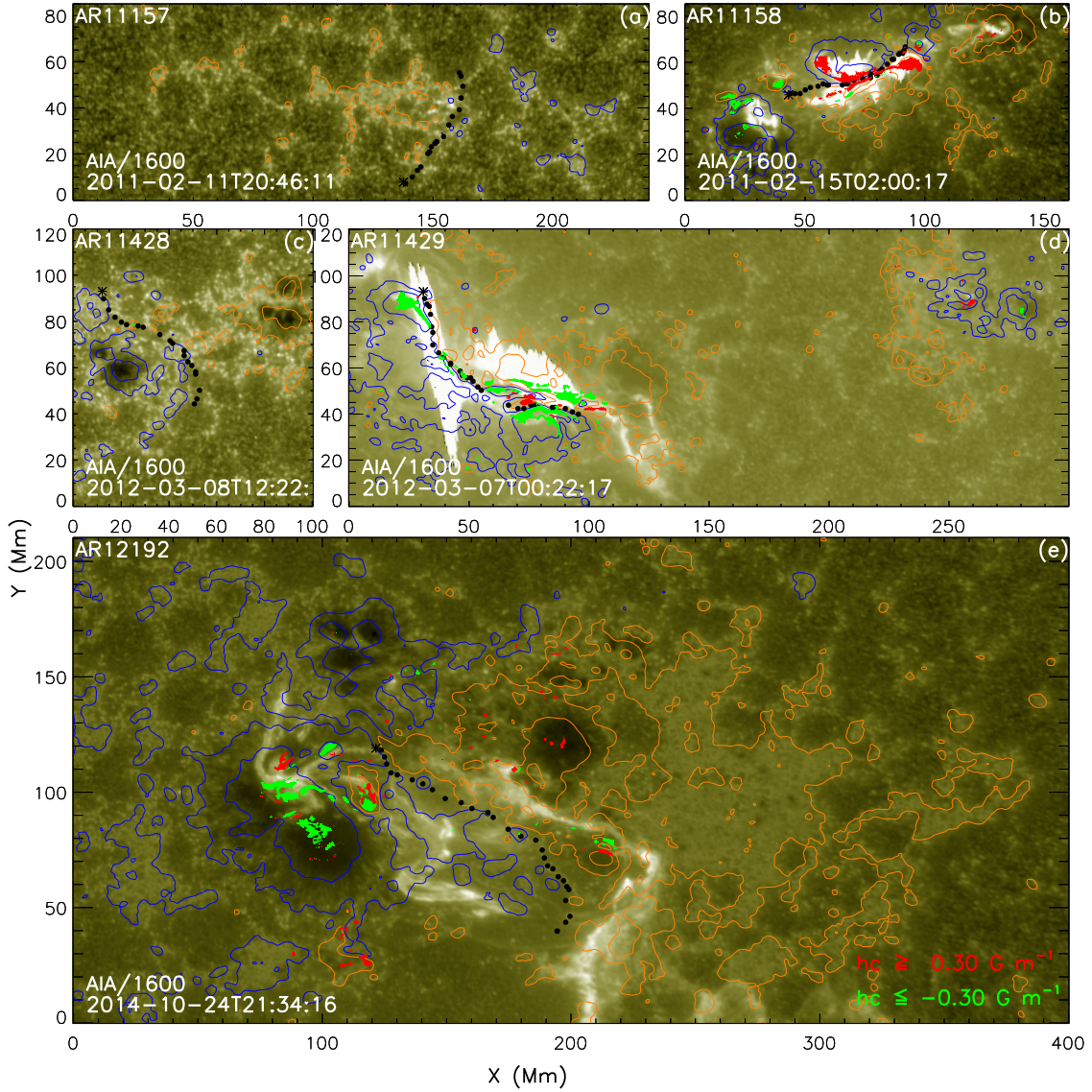


Figure 4. Distribution of current helicity h_c of the ARs at specific moments: right before the onsets of the biggest flares for ARs 11158, 11429, and 12192; and central meridian transits for ARs 11157 and 11428. The AIA/1600 Å images near the flares' peaks are plotted as background. The B_r component of the field is contoured on the images: orange contours for a positive B_r of 200, 1000 Gauss, blue contours for a negative B_r of -200 , -1000 Gauss. Red patches are for $h_c \geq 0.3 \text{ G}^2 \text{ m}^{-1}$ and green ones for $h_c \leq -0.3 \text{ G}^2 \text{ m}^{-1}$. Black dotted lines show the paths along the flaring neutral lines or the main polarity inverse lines (if there was no flare), above which we calculated the decay index. The panels (a)–(e) are for ARs 11157, 11158, 11428, 11429, and 12192, respectively.

Table 4
Current Helicity and Magnetic Flux in Strong h_c Regions in Different Polarities^a

AR No.	Parameters in all strong h_c pixels				R^Φ	Parameters in strong h_c pixels of dominant sign				
	$H_{\text{total}}^t (\text{G}^2 \text{ m}^{-1})$		$\Phi^t (10^{21} \text{ Mx})$			$H_{\text{dc}}^t (\text{G}^2 \text{ m}^{-1})$		$\Phi_d^t (10^{21} \text{ Mx})$		R_d^Φ
	in $\mathcal{P}_{B_z > 0}$	in $\mathcal{P}_{B_z < 0}$	in $\mathcal{P}_{B_z > 0}$	in $\mathcal{P}_{B_z < 0}$		in $\mathcal{P}_{B_z > 0}$	in $\mathcal{P}_{B_z < 0}$	in $\mathcal{P}_{B_z > 0}$	in $\mathcal{P}_{B_z < 0}$	
11158	885.70	674.69	2.11	-2.24	1.06	625.86	441.28	1.64	-1.46	1.12
11429	964.28	1642.08	2.83	-4.47	1.58	-732.27	-1381.21	2.24	-3.83	1.71
12192	1307.59	1988.95	3.58	-9.23	2.58	-589.88	-1385.31	1.49	-6.95	4.67

Notes. Strong h_c regions refer to pixels where $|h_c| \geq 0.3 \text{ G}^2 \text{ m}^{-1}$. Quantities are calculated by: $H_{\text{total}}^t = \Sigma^t |B_z (\nabla \times B)_z|$; $H_{\text{dc}}^t = \Sigma_d^t B_z (\nabla \times B)_z$; $\Phi^t = \Sigma^t B_z dA$; $\Phi_d^t = \Sigma_d^t B_z dA$. R^Φ is the larger ratio between $|\Phi^t|/|\Phi_d^t|$ in different polarities. Superscript t refers to threshold ($0.3 \text{ G}^2 \text{ m}^{-1}$ here) of h_c ; subscript d refers to the dominant sign of h_c .

^a $\mathcal{P}_{B_z > 0} (\mathcal{P}_{B_z < 0})$ refers to positive (negative) polarity.

The current helicity and magnetic flux in the strong h_c region of the three productive ARs are listed in Table 4. For all pixels where $|h_c| \geq 0.3 \text{ G}^2 \text{ m}^{-1}$, the R^Φ of ARs 11158 and 11429 are

not larger than 1.6, indicating a rough balance between the positive and negative magnetic flux in those regions; the R^Φ of AR 12192 is 2.58, indicating a stronger flux imbalance.

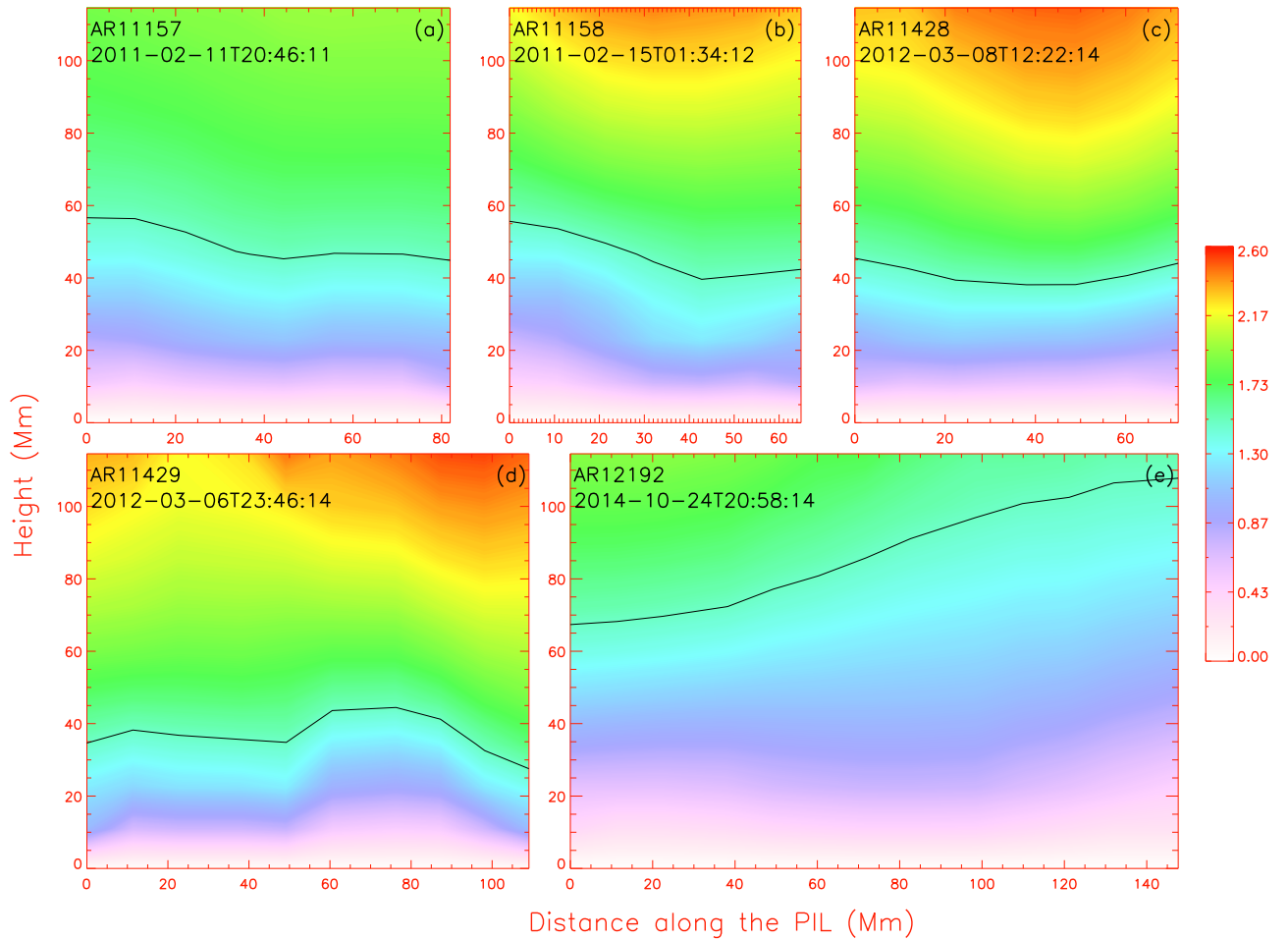


Figure 5. Distribution of the decay index above the flaring neutral lines of ARs 11158, 11429, and 12192 before the onset of their largest flares (panels (b), (d) and (e)), or above the polarity inverse lines of ARs 11157 and 11428 at their central meridian transits (panels (a) and (c)). The black lines mark the position where n reached the critical value of 1.5.

Furthermore, an AR usually has a dominant current helicity sign, as indicated by $\overline{H_c}$ in Figure 2 and Table 1, which is positive for AR 11158, and negative for ARs 11429 and 12192. It may refer to a dominant handedness of twist or shear in an AR. Thus we introduce another ratio, R_d^ϕ , similar to R^ϕ but only for the pixels where $|h_c|$ is greater than the threshold in the dominant sign. The R_d^ϕ of AR 12192 is 4.67, which is much larger than the value of ARs 11158 and 11429, showing a stronger flux imbalance between the strong h_c regions in both polarities. These results suggest that there might be no mature sheared or twisted core field in AR 12192, and the large value of $H_{c\text{total}}$ shown in Figure 2(c) could be a result of the large area of the AR. For the two inert ARs, 11157 and 11428, there also are no such seed structures, as exhibited by the h_c distribution. The current helicity explored here can be easily derived from the measurements of the photosphere magnetic field, and could be a useful parameter for space weather forecasting.

4.2. Decay Index

Furthermore, the pre-existing core field may be constrained by the external field. We checked the decay index of the ARs to discover the constraint above them. Decay index is defined by $n = -\frac{d \ln B_{\text{ex}}(h)}{d \ln h}$, in which h is the height from the solar surface, and B_{ex} is the external field above the AR. The coronal magnetic field here is the potential field extrapolated from the

SDO/HMI synoptic chart by using the potential field source surface (PFSS) model (Schatten et al. 1969; Wang & Sheeley 1992). A larger decay index means that the constraint in the corona decreases faster with increasing height, and therefore a perturbation in the lower corona may cause the CME seed to erupt out more easily (Török & Kliem 2005; Wang & Zhang 2007; Liu 2008). The critical value above which an eruption is more likely to occur is 1.5 (Török & Kliem 2007; Aulanier et al. 2010).

Figure 5 shows the spatial distribution of the decay index along the flaring neutral lines, the black lines marking the critical heights where n reaches 1.5. Clearly, the heights of ARs 11158 and 11429 where n reach 1.5 are lower than that of AR 12192, which means that the constraining field above the two ARs with eruptive flares decays more rapidly than the one with a confined flare, thus making a CME more easily. The two inert ARs, 11157 and 11428, also have relatively low critical heights, but they have no appreciable seed structures as previously pointed out. Thus there was no CME, even though the external field decayed rapidly.

5. CONCLUDING REMARKS

In this work, through comparing AR 12192 with four other ARs, we found that three parameters, the total magnetic flux (Φ), the total unsigned vertical current (I_{total}), and the proxy of

photospheric free magnetic energy (ρ_{tot}), could be responsible for the flare productivity of our sample ARs. The flare-rich but CME-poor AR 12192, similar to the other two flare-rich ARs, 11158 and 11429, has a larger Φ , I_{total} , and ρ_{tot} , which means that they are larger in size and contain a stronger current system and more free magnetic energy than the two inert ARs, 11157 and 11428. This is reasonable, as a sufficient amount of free magnetic energy is a necessary condition for an AR to power flares.

No single threshold on any parameter could be used to distinguish the flare and CME productivity of the ARs, but the combination of the mean current helicity and the total unsigned current helicity can be used to distinguish flare and CME productivity. The magnitude of the mean current helicity ($|\overline{H_c}|$) is large for the CME-rich ARs, and small for AR 12192 and the other two CME-poor ARs, while the total unsigned current helicity ($H_{c\text{total}}$) of AR 12192 is as large as the two CME-rich ARs, indicating the presence of sheared or twisted field in all three flare-productive ARs. Considering the spatial distribution of current helicity, AR 12192 has h_c concentrated in only one polarity, suggesting the absence of a mature seed structure for CME formation during flares. The CME-rich ARs can also be distinguished by the constraint of the overlying arcade field: AR 12192 has a smaller decay index than the CME-rich ARs, thus no strong CME accompanied the many intense flares it produced.

Our study here suggests that pre-existing seed structures at flaring positions might be a necessary condition for CMEs. In addition, a large decay index above the AR's flaring neutral lines, which indicates a weak constraint, may be another necessary condition for CMEs. All of these facts explain the unusual behavior of AR 12192: super flare-rich but CME-poor. This conclusion is obtained based on a sample of five ARs; its generality should be checked within a larger sample, a task which will be performed in the future.

We would like to thank our anonymous referee for the careful review and helpful comments which helped us to revise this paper. We acknowledge the use of the data from the HMI and AIA instruments on board Solar Dynamics Observatory (SDO), the MDI and LASCO instruments on board *Solar and Heliospheric Observatory (SOHO)*, and the *Geostationary Operational Environmental Satellite (GOES)*. This work is supported by grants from NSFC (41131065, 41421063, 41274173, 41574165, 41222031, and 41474151), CAS (Key Research Program KZZD-EW-01-4), MOEC (20113402110001), MOST973 key project (2011CB811403), the fundamental research funds for the central universities, and the funds of the Thousand Young Talents Programme of China (R.L).

REFERENCES

- Abramenko, V. I., Wang, T., & Yurchishin, V. B. 1996, *SoPh*, 168, 75
 Akiyama, S., Yashiro, S., & Gopalswamy, N. 2007, *AdSpR*, 39, 1467
 Amari, T., Luciani, J. F., Mikic, Z., & Linker, J. 1999, *ApJ*, 518, 57
 Aulanier, G., Török, T., Démoulin, P., & DeLuca, E. E. 2010, *ApJ*, 708, 314
 Bao, S., & Zhang, H. 1998, *ApJL*, 496, L43
 Berger, M. A., & Field, G. B. 1984, *JFM*, 147, 133
 Bobra, M. G., & Couvidat, S. 2015, *ApJ*, 798, 135
 Bobra, M. G., Sun, X., Hoeksema, J. T., et al. 2014, *SoPh*, 289, 3549
 Brown, M. R., Canfield, R. C., & Pevtsov, A. A. 1999, *Magnetic Helicity in Space and Laboratory Plasmas*, Geophysical Monograph Ser. 111 (Washington, DC: American Geophysical Union)
 Brueckner, G. E., Howard, R. A., Koomen, M. J., et al. 1995, *SoPh*, 162, 357
 Canfield, R. C., Hudson, H. S., & McKenzie, D. E. 1999, *GeoRL*, 26, 627
 Chen, A., & Wang, J. 2012, *A&A*, 543, 49
 Chen, C., Wang, Y., & Shen, C. 2011, *JGRA*, 116, A12108
 Démoulin, P. 2007, *AdSpR*, 39, 1674
 Emslie, A. G., Dennis, B. R., Shih, A. Y., et al. 2012, *ApJ*, 759, 71
 Falconer, D. A., Moore, R. L., & Gary, G. A. 2002, *ApJ*, 569, 1016
 Falconer, D. A., Moore, R. L., & Gary, G. A. 2006, *ApJ*, 644, 1258
 Feynman, J., & Hundhausen, A. J. 1994, *JGRA*, 99, 8451
 Georgoulis, M. K., & Rust, D. M. 2007, *ApJL*, 661, L109
 Green, L. M., López Fuentes, M. C., Mandrini, C. H., et al. 2002a, *SoPh*, 208, 43
 Green, L. M., Matthews, S. A., van Driel-Gesztelyi, L., Harra, L. K., & Culhane, J. L. 2002b, *SoPh*, 205, 325
 Guo, J., Zhang, H. Q., & Chumak, O. V. 2007, *A&A*, 462, 1121
 Harrison, R. A. 1995, *A&A*, 304, 585
 Hoeksema, J., Liu, Y., Hayashi, K., & Sun, X. 2014, *SoPh*, 289, 3483
 Jing, J., Song, H., & Abramenko, V. 2006, *ApJ*, 644, 1273
 Kaiser, M. L., Kucera, T. a., Davila, J. M., et al. 2008, *SSRv*, 136, 5
 Leka, K. D., & Barnes, G. 2007, *ApJ*, 656, 1173
 Leka, K. D., & Barnes, G. 2003b, *ApJ*, 595, 1296
 Leka, K. D., & Barnes, G. 2003a, *ApJ*, 595, 1277
 Lemen, J. R., Title, A. M., Akin, D. J., et al. 2012, *SoPh*, 275, 17
 Lin, J., & Forbes, T. G. 2000, *GRA*, 105, 2375
 Liu, Y. 2008, *ApJL*, 679, L151
 Liu, Y., & Schuck, P. W. 2012, *ApJ*, 761, 105
 Low, B. C. 1994, *PhPl*, 1, 1684
 Low, B. C., & Berger, M. A. 2003, *ApJ*, 589, 644
 Nindos, A., & Andrews, M. D. 2004, *ApJ*, 616, 175
 Nindos, A., Zhang, J., & Zhang, H. 2003, *ApJ*, 594, 1033
 Olmedo, O., Zhang, J., Wechsler, H., Poland, A., & Borne, K. 2008, *SoPh*, 248, 485
 Pevtsov, A. A., Canfield, R. C., & Metcalf, T. R. 1995, *ApJ*, 440, 109
 Pevtsov, A. A., Berger, M. A., Nindos, A., Norton, A. A., & van Driel-Gesztelyi, L. 2014, *SSRv*, 186, 285
RHessi science nugget no.239, http://sprg.ssl.berkeley.edu/~tohan/wiki/index.php/A_Record-Setting_CMEless_Flare
 Sammis, I., Tang, F., & Zirin, H. 2000, *ApJ*, 540, 583
 Schatten, K. H., Wilcox, J. M., & Ness, N. F. 1969, *SoPh*, 6, 442
 Schrijver, C. J. 2007, *ApJL*, 655, L117
 Schrijver, C. J. 2009, *AdSpR*, 43, 739
 Seehafer, N. 1990, *SoPh*, 125, 219
 Sun, X., Bobra, M. G., Hoeksema, J. T., et al. 2015, *ApJL*, 804, L28
 Ternullo, M., Contarino, L., Romano, P., & Zuccarello, F. 2006, *AN*, 327, 36
 Thalmann, J. K., Su, Y., Temmer, M., & Veronig, a. M. 2015, *ApJL*, 801, L23
 Tian, L., Liu, Y., & Wang, J. 2002, *SoPh*, 209, 361
 Török, T., & Kliem, B. 2005, *ApJ*, 630, 97
 Török, T., & Kliem, B. 2007, *AN*, 328, 743
 Tziotziou, K., Georgoulis, M. K., & Raouafi, N.-E. 2012, *ApJL*, 759, L4
 Valori, G., Démoulin, P., & Pariat, E. 2012, *SoPh*, 278, 347
 Wang, C., & Zhang, M. 2015, *SoPh*, 290, 811
 Wang, Y., & Zhang, J. 2007, *ApJ*, 665, 1428
 Wang, Y., & Zhang, J. 2008, *ApJ*, 680, 1516
 Wang, Y.-M., & Sheeley, N. R., Jr. 1992, *ApJ*, 392, 310
 Yashiro, S. 2004, *JGR*, 109, A07.105
 Yashiro, S., Gopalswamy, N., Akiyama, S., Michalek, G., & Howard, R. A. 2005, *JGRA*, 110, A12S05
 Yashiro, S., Akiyama, S., Gopalswamy, N., & Howard, R. a. 2006, *ApJ*, 650, 143
 Zhang, H., & Bao, S. 1998, *A&A*, 339, 880
 Zhang, H., Tian, L., Bao, S., & Zhang, M. 2000, *JApA*, 21, 245
 Zhang, M. 2006, *ApJ*, 646, 85
 Zhang, M., & Flyer, N. 2008, *ApJ*, 683, 1160
 Zhang, M., Flyer, N., & Low, B. C. 2006, *ApJ*, 644, 575